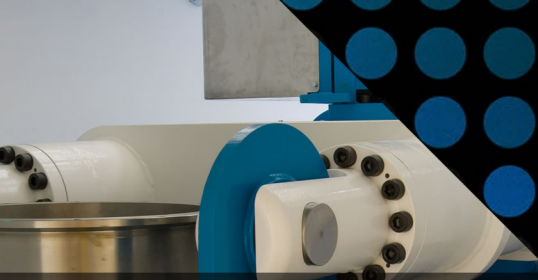

Proceedings of the Department of Civil and Structural Engineering University of Sheffield, UK

The Annual Postgraduate Research Student Conference - 2016

Edited by Harm Askes, Matthew Gilbert and Luca Susmel

Sheffield, 10th May 2016
ISBN: 9788895940656

The University Of Sheffield.

Table of Contents

Foreword

The four papers which appear in these proceedings were contributed by current research students studying in the Department of Civil & Structural Engineering at the University of Sheffield. The papers which have been included provide a flavour of the breadth of the research currently being undertaken in the Department.

Producing the present volume of papers marks a further positive development for the Department. We are confident that the research students involved will have benefited from the experience of writing up their work in the form of a conference paper.

We would like to express our heartfelt gratitude to the European Structural Integrity Society (http://www.structuralintegrity.eu) and to the Italian Group of Fracture (www.gruppofrattura.it) for supporting the publication of these proceedings.

Harm Askes
Head of Department

Matthew Gilbert
Director of Research

Luca Susmel
Postgraduate Research Tutor

Sheffield, 10 May 2016

Pounding response of buildings under earthquake motions

N. Farhadzadeh
Department of Civil and Structural Engineering, the University of Sheffield, Sheffield S1 3JD, United Kingdom
Nfarhadzadeh1@sheffield.ac.uk

Primary Supervisor: Dr Zuhal Ozdemir –Z.Ozdemir@Sheffield.ac.uk
Secondary Supervisor: Professor Andrew Tyas –A.Tyas@Sheffield.ac.uk

ABSTRACT. Simulation of structural pounding using impact element models has attracted researcher's attention for many years. This study aims at developing an impact element model which can represent the elasto-plastic pounding behavior of buildings during earthquake. This impact element model will be appropriate for modelling impact between two flat surfaces. For this purpose, Hopkinson Pressure Bar (HPB) experimental tests and non-linear finite element (FE) analysis are first conducted to investigate the contact response of different structural materials at variable loading rates. Then, existing impact element models have been applied to predict the response of experimental and numerical models. The performance of the existing impact element models particularly the linear viscoelastic model has been compared against the HPB experimental results of steel/steel impact. The results indicated that providing suitable contact parameters, the impact element models can predict the impact response of materials realistically.

KEYWORDS. Structural pounding; Hopkinson pressure bar (HPB); Contact model; Contact stiffness; Flat surface geometries; Elasto-plastic behaviour.

INTRODUCTION

Structural collision, also known as seismic pounding has been observed following many past earthquakes such as in Mexico City earthquake in 1985, Christchurch in 2011 and more recently in Gorkha earthquake in Nepal 2015. During the Mexico earthquake, 3% to 4.5% of buildings were extensively damaged/ collapsed due to pounding. One of the great buildings which collapsed due to pounding was the De Carlo Hotel which was insufficiently distanced from its neighboring building. As a result of ground excitation, buildings were induced to apply hammer like forces on one another leading to a great horizontal failure in the middle of the De Carlo Hotel building. Studies [1, 2] on seismic vulnerability of structures have recognized pounding as one of the main hazards for structures. Five different configurations of buildings have been described [1] as being the most susceptible to pounding during earthquake motions; (i) adjacent to a building with shorter stories (ii) closely spaced to a large-massed structure (iii) mid-column pounding (iv) being at the end of a raw of several adjacent structures, and (v) eccentric pounding. In addition to the five configurations, adjacent buildings with different set-backs are also known to be vulnerable to pounding.
Regular observation of structural pounding and its resultant damages/collapses have led to an extensive body of literature since 1980s. It started from analysis of structures modelled as single-degree-of-freedom systems [3, 4] and soon the investigation was taken further on to the analysis of multi-storey structures [5, 6]. Structural pounding behavior during earthquakes is mainly simulated using two approaches; (1) the Stereomechanics approach which is based on the conservation of momentum law, (2) impact element models which directly simulates the pounding forces.

Several experimental tests such as shaking table tests, pendulum tests, and dropping ball tests [7, 9] have been conducted to investigate pounding. Three-dimensional analyses of structural longitudinal, transversal and torsional pounding also exist in the literature [10-14]. Anagnostopoulos [3]; Anagnostopoulos & Spiliopulos [6] and; Muthukumar & DesRoches [7] idealized structures as lumped masses and investigated the effect of contact stiffness and energy loss on the adequacy of impact element models. Khatiwada [15] idealized two segments of a bridge as distributed mass models to observe the influence of stress propagation and the resultant deformation in the impacted bodies. Cole et al [16] studied the wave theory which is the base theory of distributed mass models as well as the disadvantages of the theory in simulating the contact stresses amplitudes and durations for different structural materials. Khatiwada [11] was the first to introduce the Sears model for simulation of structural pounding. The model is a distributed mass model which accounts for contact forces thorough the deformation caused by the propagation of contact stress waves through the impacted bodies.

For the past two decades, several impact element models such as the linear or non-linear elements (Hertz model), linear or non-linear viscoelastic elements (Kelvin-Voight model) are used to assess pounding forces. The linear spring element is the simplest link element which becomes activate once the two bodies come into contact. However, this model over-estimates the pounding forces as there is no dashpot assumed in the system to account for energy loss. In contrary with linear elastic element, the linear and non-linear viscoelastic link elements include a dashpot to take into account the energy dissipation. However, one of the main disadvantages of linear viscoelastic model is the assumption of uniform energy dissipation throughout the whole time of contact. In general, these models are found to be reasonable in simulating the structural responses. However, still diverse results can be obtained when all these impact element models are applied to a single structural pounding situation which is due to the great dependency of these models on some of the contact parameters [17]. As an example, Muthukumar & DesRoches [7] has found the significant effect of the coefficient of restitution whereas Anagnostopoulos [3] found it to be insignificant.

Due to these uncertainties associated with contact parameters, simulation of structural pounding using these impact element models can sometimes be unrealistic [15]. Nevertheless, there is still a reasonable prediction of pounding forces is required to design devices such as viscous damping to restrict structural movements and minimize the possible pounding damage. However, to prevent pounding of adjacent buildings there should be at least some amount of distance between them. Therefore, the current practice codes determine a minimum distance between the two structures to prevent them from pounding which is easier rather than dealing with the post-earthquake damages. However, there still exist structures with no separation gaps; as an example in Iran, in most of the cities centers, many structures are built extremely close to each other and their structural systems do not allow connecting them together. Also in many large cities, lack of land and the cost of it as well as architectural restrictions do not allow structural engineers to leave sufficient gaps between structures. Therefore, it is essential to have precise measurements of pounding forces for the existing adjacent structures built in such earthquake prone countries.

RESEARCH AIM

The aim of this research is to develop an impact element model, which can represent elasto-plastic contact phenomenon occurring due to pounding of structures during earthquakes. The developed impact element will be appropriate for modelling impact between two flat surfaces. In addition, appropriate contact stiffness and damping parameters of the developed impact element model will be determined to model pounding phenomenon occurring between two RC buildings, two steel buildings, or one steel and one RC building. To accomplish this aim, HPB tests and non-linear FE analysis are performed to collect more data on the contact response of materials at different loading rates. A new impact element model will be developed based on HPB numerical simulation and experimental tests. The developed impact element model will be validated by finite element modelling of pounding between two single-storey buildings.

METHODOLOGY OF CURRENT RESEARCH

Preliminary numerical analysis

Preliminary numerical analysis was conducted in ANSYS-LS DYNA to simulate impact between different structural materials. The preliminary analysis provided the opportunity of understanding the stress wave propagation and the material behavior during impact. These numerical analyses were used to determine the specimen's measurements and the striker's velocities and other necessary information for setting up the Hopkinson Pressure Bar tests. Impact was

modelled between two free axi-symmetric bars and a specimen which was attached to the front of the striker for steel to steel, and concrete to steel impacts. However for concrete to concrete impacts, the specimens were placed at the front of Hopkinson bar which was to prevent any damage to the Bar. The bars were modelled using shell elements with mesh size of 1 mm. HPB setup is shown in Figure 1. For modelling HPB steel/steel impact, the simplified Johnson Cook material model (MAT 15) was used and for concrete/concrete impacts, the continuous surface cap material model (MAT 159) was used in ANSYS-LSDYNA. Variable impact velocities ranging from 0.80 m/s to 26.60 m/s were determined using the numerical model of HPB. Some of the chosen velocities for concrete/concrete impact were so high that caused total failure of the concrete specimens as well as some of the concrete strikers in the experiment. The specimen's lengths were 25, 50, and 100 mm with diameter of 50 mm. The lengths of the steel and concrete strikers were 400 mm with diameter of 50 mm for all tests. However the HPB diameter was 49.2 mm. The material properties of the HPB were taken from [18] and are shown in table 1. To compare the performances of the existing impact element models, parametric study was conducted using the force-displacement response of materials during HPB experimental tests. From the obtained force-displacement data, contact stiffness and the coefficient of restitution values for each test were determined. Several impact element models such as the non-linear and linear viscoelastic, linear and non-linear elastic, non-linear Hertz-damped and linear Hunt and Crossley models were compared against the experimental test results of HPB.

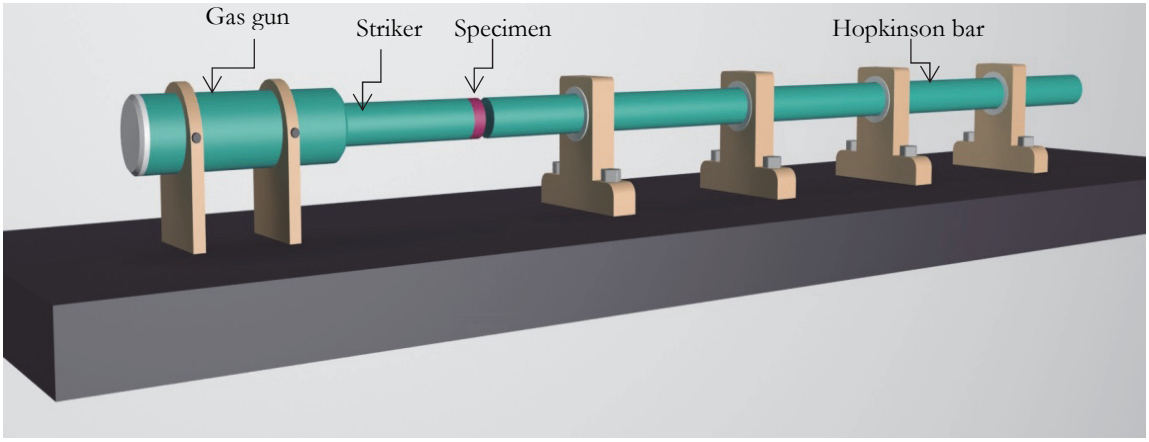

Figure 1: HPB set up.

HPB measurements and material properties	
Length and radius of HPB	5.850 m and 0.0246 m (+/- 0.00005 m)
One dimensional wave velocity (C_0)	5194 m/s (+/- 13 m/s)
Density (ρ)	7850 kg/m^3
Elastic modulus (E)	212×10^9 N/m^2 (+/- 1.5×10^9 N/m^2)
Poisson's ratio (ν)	0.29

Table 1: Properties of the Hopkinson Pressure Bar used in the experiment.

Even though all of these models were originally developed for impact between sphere/sphere and flat/sphere surfaces, they still provided reasonable results for impact of bars with flat surface geometries. The contact stiffness value for each model was modified to simulate similar forces to the HPB numerical results. The coefficients of restitution values were found to have a negligible effect on the performances of the existing impact element models. For the sake of brevity, only one of the results of the comparison between the HPB numerical simulation and the linear viscoelastic model has been provided in this paper. It should be noted that for the linear viscoelastic impact element models, displacement-time histories were obtained from the HPB numerical analysis. Providing correct contact stiffness and damping ratio/constants values as well as displacement-time histories, the impact model was quite reasonable in simulating the impact forces. Figure 2 shows the comparison of the performance of linear viscoelastic model with the HPB numerical impact model of steel to steel with an impact velocity of 5 m/s. The contact stiffness and the coefficient of restitution values for this impact were $K = 8 \times 10^9$ N/m and $e = 0.07$.

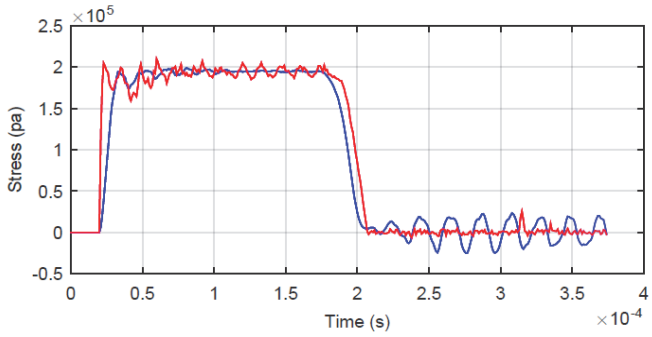

Figure 2: Comparison of linear viscoelastic model (blue line) with HPB numerical analysis result (red line) for impact of steel to steel with an impact velocity of 5 m/s; Steel specimen length and diameter 25 mm and 50 mm; Hopkinson bar length and dimeter were 5850 mm and 49.2 mm; striker length and diameter were 400 mm and 50 mm

Contact of bars with spherical surface geometries

In addition to the investigation of contact between two flat surfaces, contact between bars made with spherical surface geometries was also modelled. Force-displacement curve obtained from the numerical model of HPB was compared against the force-displacement curve obtained from the Hertz model. Both force-displacement curves showed excellent agreement. The contact stiffness value calculated using the Hertz contact stiffness formula was determined to be $K = 1.72 \times 10^{10}\,\mathrm{N/m^{3/2}}$. However, this value did not provide a reasonable contact force-displacement curve because when the Hertz contact stiffness value was used the impact maximum contact force was smaller than the maximum force obtained from the numerical model. Therefore, the contact stiffness value was modified to $K = 3.17 \times 10^{12}\,\mathrm{N/m^{3/2}}$. The new K value provided a force-displacement curve which perfectly agreed with the contact force obtained from the numerical model.

HPB experimental tests and the verification of the numerical impact model of two steel bars

Six numbers of HPB experimental tests were conducted on the impact of steel/steel with specimen's length of 25 mm, concrete to steel with concrete specimen's approximate lengths of 25, 26, 51, and 52 mm, and concrete to concrete impacts with specimen's length of approximately 26 mm. The impact velocity for steel/steel impact was 19.4 m/s, for concrete to steel were 0.8, 6.5, 8.15, 18.88 m/s, and for concrete to concrete impact was 26.6 m/s. Comparison of stress-time histories obtained from the HPB experimental tests and its FE numerical model for steel to steel impact with an impact velocity of 19.4 m/s is illustrated in Figure 3. Also Figures 4 and 5 show the stress-time histories obtained from the HPB experimental test on concrete to steel, and concrete to concrete impacts.

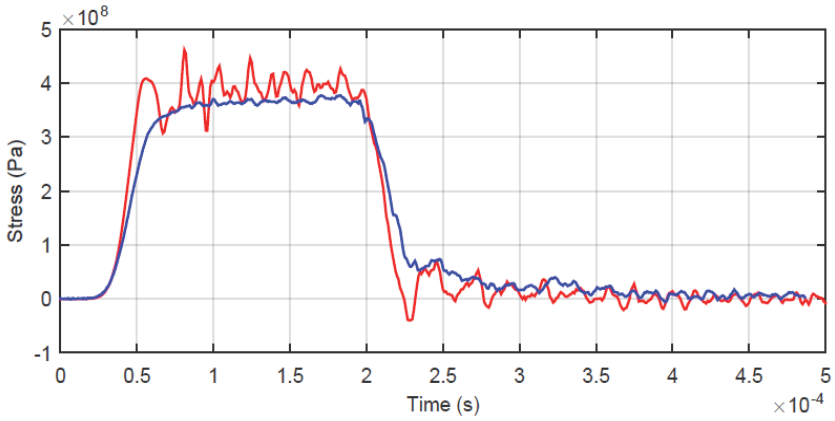

Figure 3: Comparison of the HPB numerical model (red line) with HPB experimental test (blue line) for steel to steel impact with an impact velocity of 19.20 m/s; Specimens length and diameter were 25 mm and 50 mm

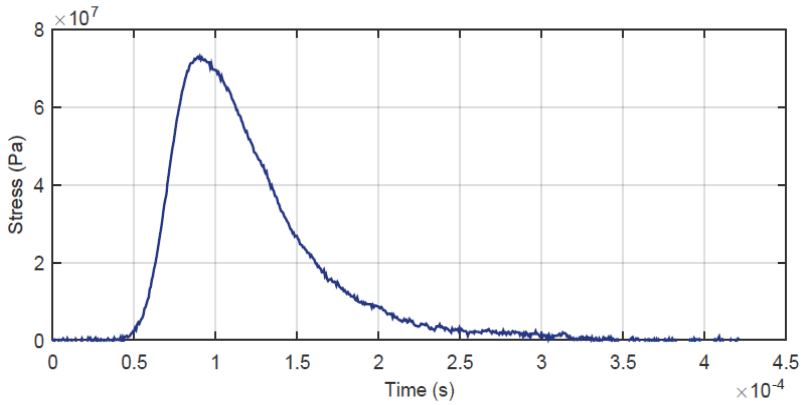

Figure 4: Stress-time history of concrete to concrete HPB experimental impact test with impact velocity of 26.6 m/s

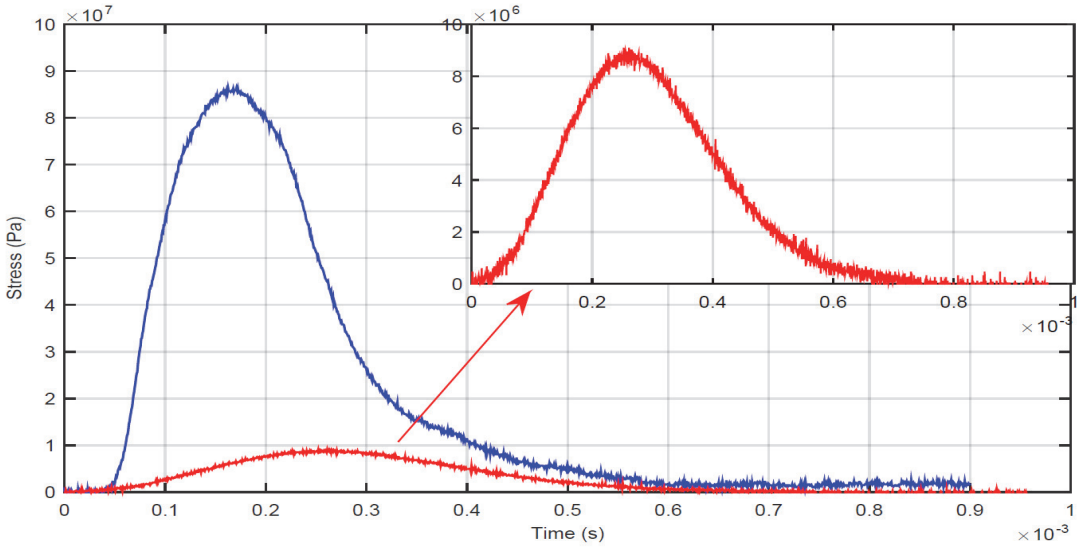

Figure 5: Comparison of stress-time histories obtained from HPB concrete to steel impact test with an impact velocity of 0.8 m/s (fully elastic- red line) with stress-time history obtained from fully crushed concrete specimen with an impact velocity of 18.88 m/s (fully plastic- blue line) - The magnified stress-time history shown in the upper right corner of the figure belongs to the elastic impact test

CONCLUSIONS

In this study HPB preliminary numerical analysis was conducted to determine HPB experimental set-ups. Impact was modelled between two steel bars, two concrete bars, and one concrete and one steel bar. Using the simplified Johnson-Cook material model, steel/steel HPB numerical model was verified against the experimental tests. Also for verification of concrete/concrete numerical model, continues surface cap model (MAT159) was used in LS-DYNA. Using the HPB experimental tests as well as the FE numerical analysis results; limited parametric study was conducted to obtain suitable contact parameters for different structural materials. With the obtained contact parameters such as the contact stiffness and the damping ratio, performance of the linear viscoelastic model was compared against the numerical results of HPB steel/steel impact. It was observed that providing correct values for contact stiffness and damping ratio/constant, as well as displacement-time histories, linear viscoelastic model is adequate enough to predict the contact forces for impact of flat surfaces even though the model was originally developed for contact of spherical/spherical and flat/spherical surfaces. However, for the development of a novel impact element model for flat surfaces, with the aid of HPB numerical analysis as well as the experimental tests, more parametric study is necessary to determine appropriate elastic and elasto-plastic contact parameters for impacts of concrete/concrete, steel/steel, and concrete/steel.

REFERENCES

[1] Jeng, V., and Tzeng, W., Assessment of seismic pounding hazard for Taipei City, Engineering Structures, 22(5) (2000) 459-471.

[2] Bothara, J.K., Jury, R.D., Wheeler, K. & Stevens, C., Seismic Assessment of Buildings in Wellington: Experiences and Challenges.In Proceedings of the 14th World Conference on Earthquake Engineering, October 12-17, (2008). Beijing, China.

[3] Anagnostopoulos, S. A., Pounding of buildings in series during earthquakes, Earthquake Engineering and Structural Dynamics, 16(3) (1988) 443-456.

[4] Athanassiadou, C. J., Penelis, G. G. and Kappos, A. J., Seismic response of adjacent buildings with similar or different dynamic characteristics, Earthquake Spectra, 10(2) (1994) 293-317.

[5] Papadrakakis M., Mouzakis H., Earthquake simulator testing of pounding between adjacent buildings. Earthquake engineering and structural dynamics. 24 (1995) 811-834.

[6] Anagnostopoulos, S. A. and Spiliopoulos, K. V., An investigation of earthquake induced pounding between adjacent buildings, Earthquake Engineering and Structural Dynamics, 21(4) (1992) 289-302.

[7] Muthukumar, S., DesRoches. R. A., Hertz contact model with non-linear damping for pounding simulation. *Earthquake engineering and structural dynamics*. 35(1) (2006) 811-828.

[8] Van Mier, J.G.M., Pruijssers, A.F., Reinhardt, H.W., Monnier, T., Load-time response of colliding concrete bodies. Journal of structural engineering.1 (1997) 354-374.

[9] Zhu P, Abe M, Fujino Y., Modelling three-dimensional non-linear seismic performance of elevated bridges with emphasis on pounding of girders. Earthquake Engineering and Structural Dynamics; 31 (2002) 1891–1913.

[10] Mouzakis, H. P. and Papadrakakis, M., Three dimensional nonlinear building pounding with friction during earthquakes, Journal of earthquake engineering, 8(1), (2004) 107-132.

[11] Jankowski, R., Earthquake induced pounding between equal height buildings with substantially different dynamic properties, Engineering Structures, 30(10) (2008) 2818-2829.

[12] Jankowski, R., Non-linear FEM analysis of earthquake-induced pounding between the main building and the stairway tower of the Olive View Hospital, Engineering Structures, 31(1) (2009) 1851-1864.

[13] Jankowski, R., Non-linear FEM analysis of pounding-involved response of buildings under non-uniform earthquake excitation, Engineering Structures, 37(0) (2012) 99- 105.

[14] Rajaram, C., Ramancharla., Three dimensional analysis of pounding between adjacent buildings. Journal of Structural Engineering.41(2) (2014) 161-171.

[15] Khatiwada, S., A distributed mass model with end-compliance effects for simulation of building pounding. University of Auckland, New Zealand (2014).

[16] Cole, G.L., Dhakal, R.P, Carr, A.J., Bull, D.K. In: The effect of diaphragm wave propagation on the analysis of pounding structures. In: M. Papadrakakis, N. D. Lagaros, and M. Fragiadakis: ECCOMAS Thematic Conference on Computational Methods in Structural Dynamics and Earthquake Engineering, 2009 Greece. Rhodes Ireland.

[17] Khatiwada, S., Chouw, N, Larkin, T., In: Simulation of structural pounding with the Sears impact model. In: M. Papadrakakis, N. D. Lagaros, V.Plevris: 4th ECCOMAS Thematic Conference on Computational Methods in Structural Dynamics and Earthquake Engineering; Jun/12-14/2013; Greece. Kos Ireland.

[18] Tyas, A., Watson, A.J., Experimental evidence of Pochammer-Chree strain variations in elastic cylinders. Experimental Mechanics. University of Sheffield. (2000) 331- 337.

Modal decomposition of instabilities in thin-walled structural elements

X. Li, J. Becque
Department of Civil and Structural Engineering, the University of Sheffield, Sheffield S1 3JD, United Kingdom
xli52@sheffield.ac.uk; j.becque@sheffield.ac.uk

Primary Supervisor: Jurgen Becque – e-mail: j.becque@shef.ac.uk
Secondary Supervisor: Buick Davison – e-mail: j.davison@shef.ac.uk

ABSTRACT. The paper presents the development of a new method for the decomposition of any deformed shape of a buckled thin-walled structural member into the contributions of a number of predefined classes of modes. In this method, these classes encompass five types, namely the local, distortional, global, transverse extension and shear modes. The modal decomposition process involves two steps. First, the transverse extension modes are separated out by enforcing the null-transverse-stress criterion. Second, the basis vectors of the local, distortional, global and shear spaces are obtained by either minimizing or maximizing the contributions of the bending energy and membrane energy in the total strain energy.

KEYWORDS. Thin-walled; Modal decomposition; Buckling modes.

INTRODUCTION

Thin-walled steel structures are enjoying an ever increasing popularity in the construction industry due to their high strength-to-weight ratio, straightforward manufacturing process and unrivalled speed of construction. Despite their appealing advantages, they are highly susceptible to instabilities due to their limited wall thickness. These instabilities, which in their 'pure' forms are often categorized as local, distortional and global modes, usually occur in combinations with significant interaction. For the purpose of both theoretical study and design, however, it is desirable to identify the contributions of the pure modes in the failure mechanism. Over the past decades two methods of modal decomposition have been proposed, which include Generalised Beam Theory (GBT) and the Constrained Finite Strip Method (cFSM). GBT was initially introduced by Schardt, R. [1,2] and can be seen as an extension of the classical theories of bending and torsion to include local and distortional deformations. Partially inspired by GBT, Ádány and Schafer [3-8] developed the cFSM, which is a modal decomposition method based on the Finite Strip Method (FSM). In this paper, a new modal decomposition method is proposed, which does not rely on the idealized assumptions of GBT. Although more generally valid, the method is here implemented in the framework of the FSM.

FSM ESSENTIALS

The finite strip method (FSM) can be seen as a specialised finite element method (FEM) dealing with prismatic thin-walled structural members. In this method, only cross-sectional discretisation is required, while sinusoidal shape functions are used longitudinally. At the minimum level, the cross-section is discretised into flat plates at the main nodes, although each flat plate can be further discretised into smaller strips using sub nodes to improve accuracy.

Main nodes associated with only one strip are called external main nodes, as opposed to internal main nodes, which connect two or more strips. These definitions are illustrated in Figure 1.

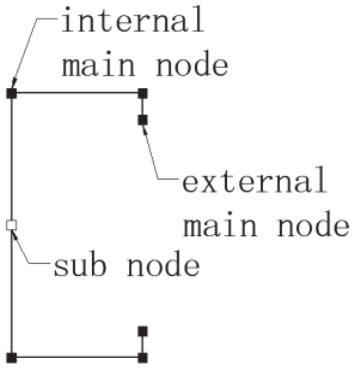

Figure 1: Definitions of node types.

In the FSM, a global coordinate system is defined, as well as a local coordinate system associated with each strip, as shown in Figure 2 (a).

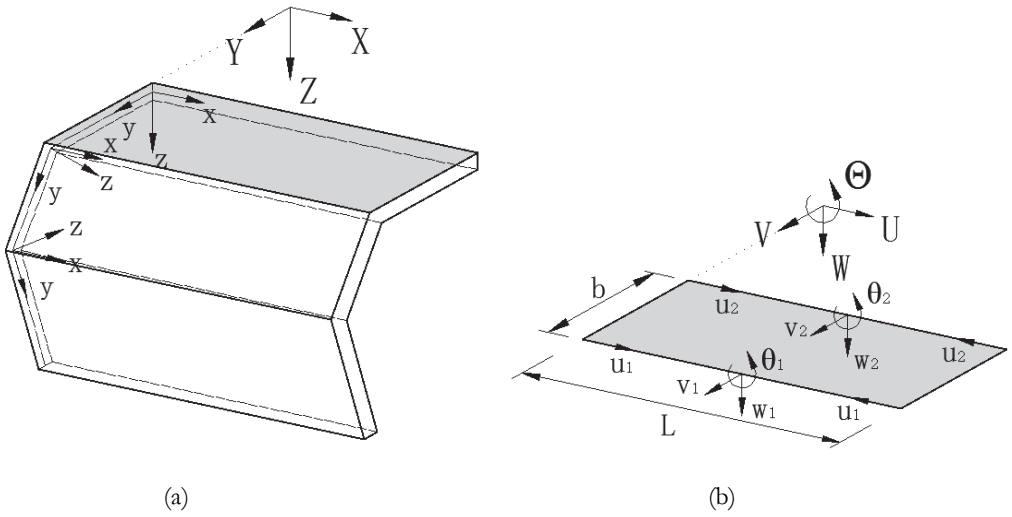

(a) (b)

Figure 2: Coordinate systems and degrees of freedom.

In the local coordinate system of each strip, each nodal line has four degrees of freedom (DOF): the longitudinal and transverse in-plane displacements u and v, the out-of-plane displacement w and the out-of-plane rotation (about the local x-axis) θ. In the global coordinate system, the corresponding DOFs are the longitudinal end displacement U, the translations V and W in the global Y and Z directions and the rotation about the X axis Θ. Figure 2(b) shows an isolated strip with its degrees of freedom. L is the length of the strip (and the member), while b is the strip width.
In the FSM, the buckling modes $\boldsymbol{d}$ of the member (which may be coupled modes rather than pure modes) are obtained by solving the following eigenvalue problem:

$$(\boldsymbol{K} - \lambda \boldsymbol{G})\boldsymbol{d} = 0 \qquad (1)$$

where the eigenvalues λ are proportional to the buckling stresses and $\boldsymbol{K}$ and $\boldsymbol{G}$ are the global elastic and geometric stiffness matrices, respectively.

MODAL DECOMPOSITION

The modal decomposition process involves two steps. First, the transverse extension modes are separated out by enforcing the null-transverse-stress criterion. Second, within the remaining space the basis vectors of the local, distortional, global and shear spaces are obtained by either minimizing or maximizing the contributions of the bending energy versus the membrane energy in the total strain energy.

Number of modes

In this paper, (uncoupled) buckling modes are categorized into five classes: local, distortional, global, transverse extension and shear modes. Each class contains a well-defined number of modes, as listed in Table 1 for the case of an open cross-section. The total number of nodes is thereby indicated by n, while n_m is number of internal main nodes and n_s is the number of strips. The readers is referred to [9] for a detailed explanation.

Mode type	Number of modes
Local	$2n - n_m$
Distortional	$n_m - 2$
Global	3
Transverse extension	$n_s = n - 1$
Shear	n

Table 1: Number of modes.

Step 1

The null-transverse-stress criterion $\sigma_y = 0$ is used to isolate the transverse extension modes from the other modes. However, due to the particular choice of the shape functions in the FSM, this condition can only be applied 'on average' over the strip: $\bar{\sigma}_y = 0$, where:

$$\begin{aligned}
\bar{\sigma}_y &= \frac{E}{1-\nu^2}\left(\varepsilon_y + \nu\bar{\varepsilon}_x\right) = 0 \\
\varepsilon_y &= \frac{\partial v}{\partial y} = \frac{v_2 - v_1}{b}\sin\left(\frac{\pi x}{L}\right) \\
\bar{\varepsilon}_x &= \frac{\partial u}{\partial x} = -\bar{u}\left(\frac{\pi}{L}\right)\sin\left(\frac{\pi x}{L}\right) \\
&= -\frac{u_1 + u_2}{2}\left(\frac{\pi}{L}\right)\sin\left(\frac{\pi x}{L}\right)
\end{aligned} \tag{2}$$

Written in terms of the global displacements, Eq. (2) becomes:

$$\frac{\left(V_1^i - V_2^i\right)\cos\alpha^i + \left(W_1^i - W_2^i\right)\sin\alpha^i}{b^i} + \frac{U_1^i + U_2^i}{2}\nu\left(\frac{\pi}{L}\right) = 0 \qquad i = 1\ldots n_s \tag{3}$$

where the superscript i refers to the i^{th} strip and α is the angle measured from the local y axis of the i^{th} strip to the global Y axis. Eq. (3), when written for all strips, can be summarised in matrix form as:

$$\boldsymbol{C}\boldsymbol{d} = \boldsymbol{0} \tag{4}$$

Therefore, a matrix containing a set of column basis vectors of the combined local, distortional, global and shear space is obtained by finding the null space of $\boldsymbol{C}$:

$$\boldsymbol{H}_{ldgs} = null(\boldsymbol{C}) \tag{5}$$

We wish to impose the additional requirement that all local, distortional, global, shear and transverse extension modes are orthogonal to each other, where orthogonality (by choice) is defined with respect to the $\boldsymbol{K}$ matrix. The full set of modes then constitutes an orthogonal basis of the whole deformation space. Orthogonality of the transverse extension modes with respect to the remaining modes requires:

$$\boldsymbol{H}_{ldgs}{}^{T}\boldsymbol{K}\boldsymbol{d}_{te} = \boldsymbol{0} \tag{6}$$

Thus, the matrix containing the basis vectors of the transverse extension space is obtained as follows:

$$\boldsymbol{H}_{te} = null\left(\boldsymbol{H}_{ldgs}{}^{T}\boldsymbol{K}\right) \tag{7}$$

Once the basis vectors of a space are obtained, the actual buckling modes under a given loading can be obtained from the constrained eigenvalue problem [9]:

$$\left(\boldsymbol{H}_{te}^{T}\boldsymbol{K}\boldsymbol{H}_{te} - \lambda\boldsymbol{H}_{te}^{T}\boldsymbol{G}\boldsymbol{H}_{te}\right)\boldsymbol{a} = 0 \tag{8}$$

while the transverse extension modes are given by:

$$\boldsymbol{d}_{te} = \boldsymbol{H}_{te}\boldsymbol{a} \tag{9}$$

Step 2

The total strain energy U of a deformed thin-walled member consists of two components: the plate bending energy U_B and the membrane (in-plane) deformation energy U_M. The energies U, U_B and U_M are functions of the displacements $\boldsymbol{d}$ as follows:

$$U = \frac{1}{2}\boldsymbol{d}^{T}\boldsymbol{K}\boldsymbol{d}\ ,\ U_B = \frac{1}{2}\boldsymbol{d}^{T}\boldsymbol{K}_B\boldsymbol{d}\ ,\ U_M = \frac{1}{2}\boldsymbol{d}^{T}\boldsymbol{K}_M\boldsymbol{d} \tag{10}$$

where the matrices $\boldsymbol{K}_B$ and $\boldsymbol{K}_M$ contain the bending stiffness and the membrane stiffness components of the matrix $\boldsymbol{K}$, respectively.

The decomposition method is based on the principle, first of all, that the local buckling modes almost exclusively mobilize the plate bending deformations, with near zero contributions of the membrane deformations. As a matter of fact, in idealized cross-sections exclusively comprised of straight plates with no rounded transition zones the participation of the plate bending energy in the total energy is absolute. On the other hand, the global modes (flexural, torsional and flexural-torsional modes) have the characteristic that they mostly involve membrane deformations. However, while small, the plate bending deformations are not entirely zero in the global modes, mostly as a result of Poisson's effects. It is noted that this is usually disregarded in other decomposition methods, which consider the cross-section to undergo displacements as a rigid body in the global modes. Based on the above, the local modes can be determined by maximizing the following expression, which includes the constraint (expressed by means of a Lagrange multiplier α) that the total strain energy is equal to unity:

$$\frac{1}{2}\boldsymbol{d}^T(\boldsymbol{K}_B - \boldsymbol{K}_M)\boldsymbol{d} - \alpha\left(\frac{1}{2}\boldsymbol{d}^T\boldsymbol{K}\boldsymbol{d} - 1\right) \tag{11}$$

An analogous equation can be written for the global modes. Differentiating these equations with respect to the degrees of freedom contained in $\boldsymbol{d}$ leads to the new eigenvalue problem:

$$\left[(\boldsymbol{K}_B - \boldsymbol{K}_M) - \alpha\boldsymbol{K}\right]\boldsymbol{d} = \boldsymbol{0} \tag{12}$$

where the original Langrange multiplier now takes on the function of an eigenvalue. However, the earlier obtained transverse extension modes should be excluded from the deformations $\boldsymbol{d}$:

$$\boldsymbol{d} = \boldsymbol{H}_{ldgs}\boldsymbol{a} \tag{13}$$

resulting in:

$$\left[\left(\boldsymbol{K}_B^{ldgs} - \boldsymbol{K}_M^{ldgs}\right) - \alpha\boldsymbol{K}^{ldgs}\right]\boldsymbol{a} = \boldsymbol{0} \tag{14}$$

where

$$\boldsymbol{K}_B^{ldgs} = \boldsymbol{H}_{ldgs}{}^T\boldsymbol{K}_B\boldsymbol{H}_{ldgs},\ \boldsymbol{K}_M^{ldgs} = \boldsymbol{H}_{ldgs}{}^T\boldsymbol{K}_M\boldsymbol{H}_{ldgs} \text{ and } \boldsymbol{K}^{ldgs} = \boldsymbol{H}_{ldgs}{}^T\boldsymbol{K}\boldsymbol{H}_{ldgs}.$$

The basis vectors of the local space follow from Eqs. (13-14) with α values equal to (or very close to) 1, while the global basis vectors have α values close to -1 and the shear modes (consisting entirely of in-plane membrane deformations) have α values equal to -1. The distortional basis vectors display α values much closer to 0 and are implicitly determined by the orthogonality of the solutions of Eq. (14). Ranking the eigenvectors by α value, in combination with the information in Table 1, thus allows the basis vectors of the local, distortional, global and shear spaces to be determined. Once the basis vectors of a given space are determined, the actual buckling modes under a given loading are obtained by formulating a constrained eigenvalue problem of the form of Eq. (8). The participation of the various classes of buckling modes in a given deformed shape can then be determined on the basis of their strain energy contributions in the total strain energy.

ILLUSTRATIVE EXAMPLE

In order to illustrate the proposed method, the double-cell box section shown in Figure 3 is studied. The resulting buckling modes are shown in Table 2. The critical stresses and the modal participation of the various classes in the FSM output are plotted against the buckle half-wavelength in Figure 4.

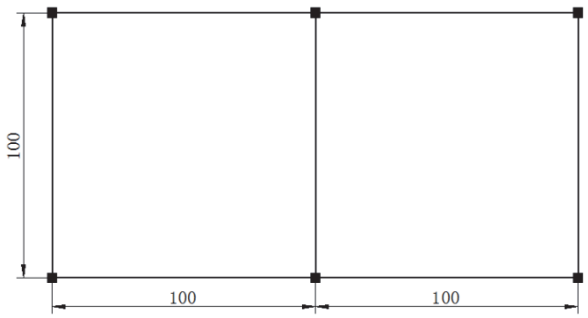

Figure 3: Double-cell box section

Table 2: Mode shapes.

CONCLUSIONS

A new approach to the modal decomposition problem is presented. Transverse extension modes are first separated from the remainder of the deformation space by imposing the null-transverse-stress criterion. Second, the participation of the plate bending energy versus the membrane deformation energy in the total energy is minimized (or maximized) to obtain the local (and global/shear) modes. The distortional modes then follow from orthogonality of the solution. The method is illustrated using an example.

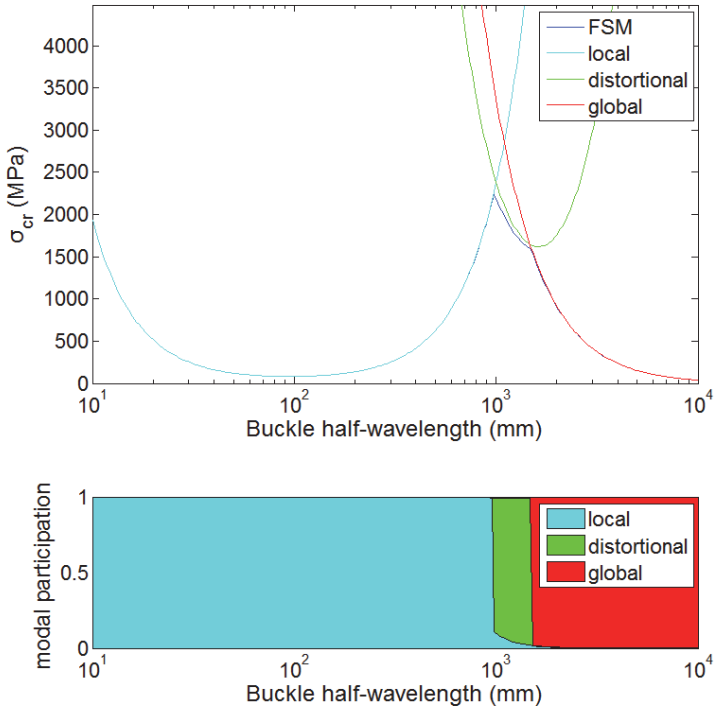

Figure 4: Critical stress and modal participation.

REFERENCES

[1] Schardt, R., Verallgemeinerte Technische Biegetheorie (generalised beam theory), Springer, Berlin, (1989).
[2] Schardt, R., Generalised Beam Theory−an adequate method for coupled stability problems, Thin-Walled Struct., 19(2-4) (1994) 161-180.
[3] Ádány, S., Schafer, B.W., Buckling mode decomposition of single-branched open cross-section members via finite strip method: Derivation, Thin-Walled Struct., 44(5) (2006) 563-584.
[4] Ádány, S., Schafer, B.W., Buckling mode decomposition of single-branched open cross-section members via finite strip method: Application and examples, Thin-Walled Struct., 44(5) (2006) 585-600.
[5] Ádány, S., Schafer, B.W., A full modal decomposition of thin-walled, single branched open cross-section members via the constrained finite strip method, J. Constr. Steel Res., 64(1) (2008) 12-29.
[6] Ádány, S., Decomposition of in-plane shear in thin-walled members, Thin-Walled Struct., 73 (2013) 27–38.
[7] Ádány, S., Schafer, B.W., Generalized constrained finite strip method for thin-walled members with arbitrary cross-section: Primary modes, Thin-Walled Struct., 84 (2014) 150-169.
[8] Ádány, S. & Schafer, B.W., Generalized constrained finite strip method for thin-walled members with arbitrary cross-section: Secondary modes, orthogonality, examples, Thin-Walled Struct., 84 (2014) 123-133.
[9] Becque, J., A new approach to modal decomposition of buckled shapes, Structures, 4 (2015) 2 – 12.

Experimental investigation of the buckling interaction between individual components of a built-up steel beam

F. Meza, J. Becque, I. Hajirasouliha
Department of Civil and Structural Engineering, the University of Sheffield, Sheffield S1 3JD, United Kingdom
fjmezaortiz1@sheffield.ac.uk; j.becque@sheffield.ac.uk; i.hajirasouliha@sheffield.ac.uk

Primary Supervisor: Dr. J. Becque – e-mail: j.becque@sheffield.ac.uk
Secondary Supervisor: Prof. J.B. Davison – e-mail: j.davison@sheffield.ac.uk

ABSTRACT. An experimental program on built-up cold-formed steel beams carried out at The University of Sheffield is presented. The specimens were assembled from plain channel sections with nominal thicknesses of 1.2 mm and 1.5 mm. The specimens were tested in a four-point bending configuration and were designed to fail by local bucking within the constant moment span. Three different connector spacings were used to study their effect on the ultimate capacity of the built-up specimens and on the way the individual sections interact with each other as they buckle. Test coupons, extracted from the corners and the flat portions of the component sections, were tested in order to determine their material properties. The out-of-plane imperfections of each built-up specimen were also recorded using a laser sensor.
The tests revealed that the interaction between the component sections is significantly affected by the connector spacing and that reducing the spacing between connectors results in an increase of the ultimate capacity.

KEYWORDS. Built-up beam; Experiment; Cold-formed steel; Stability; Local Buckling.

INTRODUCTION

The use of cold-formed steel sections as load-bearing members in structures has become increasingly popular during the past decade. It is no longer surprising to see medium-rise multi-storey buildings or cold-formed steel portal frames being constructed entirely out of cold-formed steel [1, 2]. A brief review of the recent advances and the new applications of load-bearing cold-formed steel members, with special focus on North America, has been presented in [3]. Figure 1 shows a 6-storey building constructed using a cold-formed steel framing solution, which, incidentally, is located right next to the venue where this conference is taking place. These new areas of application are putting increased demands on cold-formed structural members in term of the span length and the load-carrying capacity these members need to provide.
Due to the way cold-formed steel members are fabricated, they tend to have a mono-symmetrical or a point-symmetrical cross-section. Also, due to their typically high wall slenderness, their ultimate capacity is normally limited by buckling instabilities. These limitations are at odds with the increasing requirements which cold-formed structural members are experiencing. However, a relatively simple way to meet these new demands consists of joining two or more sections together to form a built-up section. A good example of the benefit a built-up section can provide has been reported in [4],

in which the ultimate capacity of the section constructed by joining two LiteSteel Beam (LSB) sections back-to-back was more than twice the ultimate capacity of the individual LSB sections.
In this paper an experimental program carried out on built-up steel beams, assembled by bolting four plain channels together, is described. The specimens were tested in a four-point bending configuration and were designed to fail by local buckling of their component sections along the constant-moment span. The specimens were tested with three different connector spacings and each test was repeated in order to gain increased confidence in the results.

Figure 1: 6-storey building constructed using a cold-formed steel framing system in Sheffield.

SPECIMEN GEOMETRY AND LABELING

The built-up specimens were constructed by bolting two channels of 1.5 mm thickness back-to-back, and then bolting two channels of 1.2 mm thickness to the flanges of these channels, as illustrated in Figure 2a. M6 bolts, tightened with a torque of 10 Nm, were used to assemble the specimens. All the steel sections were fabricated from pre-galvanized steel plates with a nominal yield stress of 450 MPa and a zinc coating with a nominal thickness of 0.04 mm. The built-up beams had a total length of 3400 mm, with a nominal distance between the end supports of 3000 mm. The specimens were loaded at two discrete locations, a distance of 1600 mm apart. The portion of the beam within these loading points constituted the constant moment span, while the portions of the beam which fell outside this region are referred to as the shear spans. The built-up specimens were designed with zero, two or three equally spaced connectors along the constant moment span. The spacing between the connectors along the shear spans was 100 mm for all the test specimens, as shown in Figure 2b, in order to avoid failure outside the constant moment region. The label used in this paper to refer to each of the test specimens consists of the letter 'B', followed by a hyphen and the number of rows of connectors within the constant moment span. As each test was repeated, the letters 'a' and 'b' were used to differentiate between the first and the second twin specimen tested.

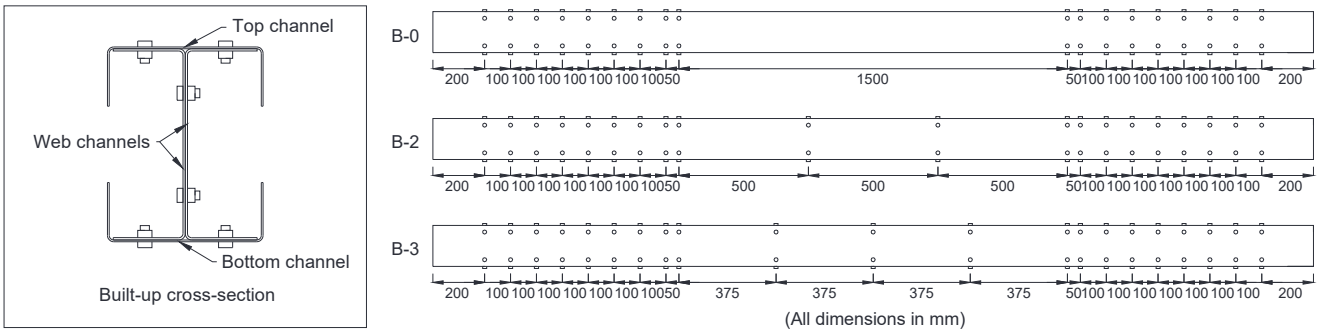

Figure 2: a) Built-up cross-sectional geometry and b) connector distribution along the constant moment and shear spans.

The cross-sectional dimensions of all the individual sections were measured prior to assembling them, and the relative positions of the components within the built-up section were recorded. Table 1 lists the measured dimensions and the

relative position of the components, with reference to Figure 2a. All reported measurements correspond to outside dimensions.

Beam	Web channel				Flange channel				Connector spacing (mm)
	location	Web (mm)	Flange (mm)	Thickness (mm)	location	Web (mm)	Flange (mm)	Thickness (mm)	
B-0a	Left	129.36	43.38	1.493	Top	104.35	39.82	1.141	1500
	Right	129.15	43.49	1.487	Bottom	104.10	39.92	1.139	
B-0b	Left	129.31	43.48	1.495	Top	104.24	39.95	1.136	1500
	Right	129.20	43.45	1.493	Bottom	104.05	39.72	1.137	
B-2a	Left	129.26	43.45	1.489	Top	103.95	39.94	1.137	500
	Right	129.13	43.53	1.496	Bottom	104.06	40.04	1.139	
B-2b	Left	128.95	43.78	1.501	Top	104.04	39.99	1.139	500
	Right	129.02	43.66	1.496	Bottom	104.01	39.97	1.144	
B-3a	Left	128.93	43.74	1.498	Top	103.95	39.98	1.141	375
	Right	128.90	43.69	1.501	Bottom	104.18	39.97	1.140	
B-3b	Left	128.83	43.70	1.506	Top	104.22	39.86	1.147	375
	Right	128.87	43.69	1.497	Bottom	103.96	39.93	1.146	
Average		129.08	43.59	1.496		104.09	39.92	1.141	-
St. Dev.		0.183	0.136	0.005		0.129	0.087	0.004	-

Table 1: Measured dimensions of the component sections.

MATERIAL PROPERTIES

The material properties of the component sections were determined by means of tensile coupons tests. As the forming process alters the mechanical properties of the virgin material (and more so with increasing cold-working), separate coupons were extracted from the flat portions and the corner regions of the individual cross-sections. More specifically, for each type of channel section used to construct the built-up geometry, two coupons were taken along the center line of the web and two more from the web-flange junction. Therefore, a total of 8 coupons were tested. The coupons were extracted from the end portions of the beams after they were tested. In this region, the level of strain the specimen experienced during the test was expected to be low enough not to affect the mechanical properties of the steel.

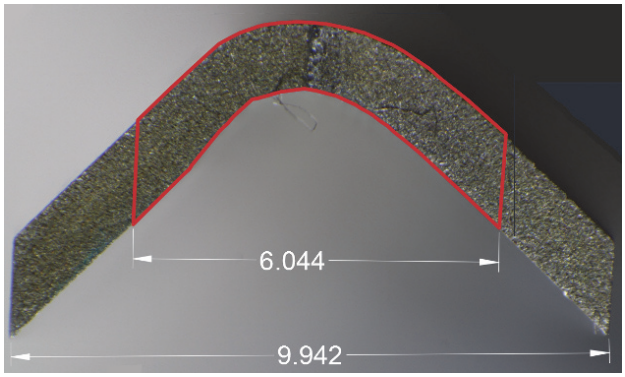

Figure 3: Photograph of the cross-section of one of the corner coupons.

In order to accurately determine the mechanical properties of the component sections (i.e. yield stress, ultimate strength and elastic modulus), special care was taken in measuring the cross-sectional area of the tensile coupons. It is stipulated in [5] that the error in determining the original cross-sectional area of a tensile coupon should not exceed ±2 %. For flat coupons, this can easily be achieved using a micrometer or caliper to measure the thickness and the width of the coupon. However, this technique is not suitable for measuring the cross-sectional area of a curved corner coupon, which was instead determined by taking a macro photograph of the cross-section with a digital camera using the reversing lens technique. The images were then imported into AutoCAD® software and scaled based on the measurement of the width of the end section of the coupon, as illustrated in Figure 3. The width of the coupon along the gauge length was also measured and drawn on the photograph, allowing the area to be calculated.
The process was repeated with pictures taken from the other end of the coupon and the average value of the areas was used. Differences in the calculated areas of less than 1.60 % and 1.94 % were obtained when using the photographs taken from each end of the corner coupons for the 1.2 mm and 1.5 mm thick channels, respectively.
All coupons were tested following the specifications given in the relevant European standard [5]. According to standard practice in the Cold-formed Steel Research Group at The University of Sheffield, the corner coupons were tested in pairs, in order to avoid the introduction of unwanted bending moments during testing [6]. Table 2 lists the average values of the Young's modulus (E), the 0.2% proof stress ($\sigma_{0.2\%}$) and the tensile strength (σ_u) obtained from each pair of twin coupons.

Type	Section	E (GPa)	$\sigma_{0.2\%}$ (MPa)	σ_u (MPa)
Flat	Flange	206	434	465
Flat	Web	206	534	622
Corner	Flange	210	459	472
Corner	Web	213	590	648

Table 2: Coupon test results.

IMPERFECTION MEASUREMENTS

The initial imperfections of the built-up specimens were recorded using the same measuring system described in [6, 7]. As the built-up specimens were designed to fail by local buckling, only the out-of-plane imperfections of those components expected to participate in local buckling were of interest. These imperfections were recorded by moving a laser sensor along several longitudinal lines, as illustrated in Figure 4. The imperfections of the web of the channels were recorded along three lines, while the imperfections of the flanges were measured along two lines. Also, as the test specimens were designed to fail within the constant moment span, only the imperfections within this region were recorded. The measured imperfections in the webs of the top channels and channels comprising the web of the built-up cross-section were smaller than 0.75 mm and 0.83 mm, respectively, while the imperfections in the flanges of the top channels were smaller than 0.66 mm.

Figure 4: Set-up used to measure the out-of-plane imperfections of the built-up specimens.

TEST SET-UP

All the built-up specimens were bent about their major axis using a four-point bending configuration, as illustrated in Figure 5. The built-up specimens were supported at the ends on rollers located 3000 mm apart. A lateral support system was used to restrain the spreader beam against any out-of-plane movement. Friction between the spreader beam and the uprights was reduced by using nylon blocks, which worked as linear bearing pads. The load, applied by a 160 kN actuator, was transmitted from the spreader beam to the test specimen through simple supports (one roller and one pin) located 1600 mm apart. These supports were also designed to restrain any out-of-plane displacement of the test specimen. Distortion of the end sections of the specimens was prevented by packing the cross-section tightly with wooden blocks.

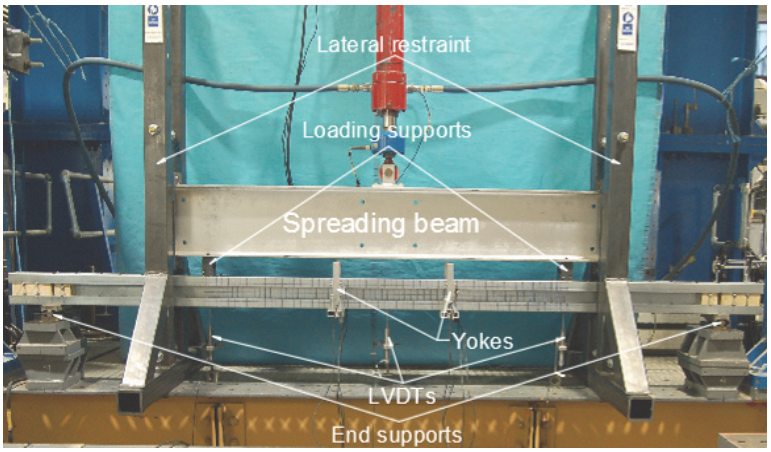

Figure 5: Four-point bending test set-up.

The vertical deflections of the built-up specimens were recorded using three LVDTs. One of them was located at mid-span, while the other two were located below the spreader beam supports. The onset of local bucking was captured by eight potentiometers mounted on two yokes supported by the bottom flange of the specimen (Figure 5).
The load was applied using displacement control at a rate of 1 mm/min. The test was continued until well into the post-buckling range.

TEST RESULTS

All specimens failed due to local buckling in the constant moment region (see Figure 6), with significant interaction taking place between the top channel and the channels comprising the web of the built-up cross-section during the test. The top channel was observed to buckle before the web channels in all test specimens. The potentiometers mounted on the yokes thereby recorded a buckled shape of the top channel which was symmetrical about the plane of bending. The web channels also buckled in a symmetrical shape with respect to the plane of bending only in those specimens without any connectors in the constant moment span. In the remaining specimens, the connectors forced the webs channels to buckle simultaneously in the same direction.
In built-up specimens B-0b, B-3a and B-3b, the buckling pattern of the top channel was seen to be significantly affected by buckling of the web channels. This interaction was most pronounced in the test specimens with three connectors, in which the flanges of the top channel were seen to invert the direction of their buckles when subsequent buckling of the web channels occurred.
Table 3 lists the ultimate capacities obtained for all test specimens, as well as the average value for each pair of twin specimens. The result of test B-0a should thereby be disregarded since the test was carried out without packing the cross-section with wooden blocks and significant lateral distortion of the end sections accompanied by in-plane bending of the top flange was observed, resulting in a slightly lower ultimate capacity. The results show that the specimens with two

connectors experienced an average increase in ultimate capacity of 2.8 % relative to the specimens without connectors, while the specimens with three connectors experienced an average increase in their ultimate capacity of 11.0 %.

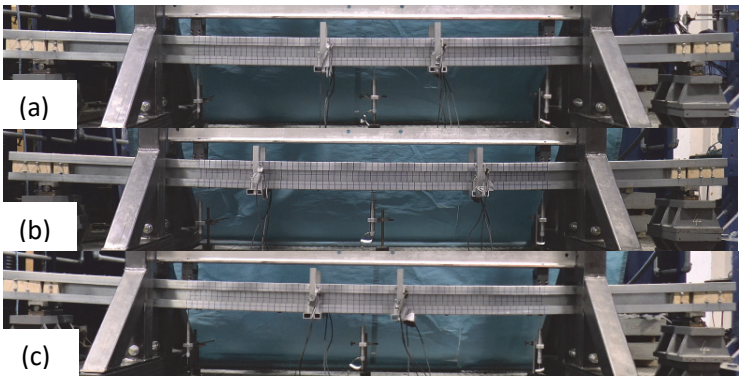

Figure 6: Buckled shape of built-up specimens a) B-0b b) B-2b c) B-3b.

Beam	Ultimate capacity (kNm)	Avg. Ultimate capacity (kNm)
B-0a	(10.56)	11.84
B-0b	11.84	
B-2a	12.51	12.17
B-2b	11.83	
B-3a	13.28	13.14
B-3b	13.01	

Table 3: Ultimate capacities of test specimens.

CONCLUSIONS

The results of an experimental program on six built-up cold-formed steel beams, tested in a four-point bending configuration, have been presented. The paper also details the procedures followed to determine the material properties and the initial out-of-plane imperfections of the specimens.
The test program revealed significant interaction between the components of the built-up specimens while buckling. This interaction was more pronounced in the specimens with shorter connector spacings. The tests also showed a relatively modest increase in the ultimate capacity of the built-up specimens when reducing the spacing between the connectors.

ACKNOWLEDGMENT

The authors gratefully acknowledge the financial support provided by the EPSRC under Grant EP/M011976/1.

REFERENCES

[1] Li Y., Shen Z., Yao X., Ma R., and Liu F., Experimental investigation and design method research on low-rise cold-formed thin-walled steel framing buildings, J. of Struct. Eng., 139 (2013) 818-836.
[2] Dundu, M., Design approach of cold-formed steel portal frames, Int. J. Steel Struct., 11 (2011) 259-273.
[3] Schafer, B. W., Cold-formed steel structures around the world, Steel Constrct. 4 (2011) 141-149.

[4] Jeyaragan, S., Mahendran, M., Experimental investigation of the new built-up LiteSteel beams, Proceedings Fifth International Conference on Thin-walled Structures, 1 (2008) 433-442.
[5] BS EN ISO 6892-1, Metallic materials – Tensile testing Part 1: Method of test at ambient temperature, British Standard Institution, (2009).
[6] Meza, F., Becque, J., Hajirasouliha, I., Experimental investigation of cold-formed Steel built-up stub columns, Eighth International Conference on Advances in Steel Structures, (2015).
[7] Meza, F., Becque, J., Experimental investigation of the buckling interaction between individual components of a built-up steel stub column, The annual Postgraduate Research Student Conference, (2015) 43-48.

Gradient elasticity: a new tool for the multiaxial high-cycle fatigue assessment of notched components

C. Bagni, H. Askes, L. Susmel
Department of Civil and Structural Engineering, the University of Sheffield, Sheffield S1 3JD, United Kingdom
c.bagni@sheffield.ac.uk; h.askes@sheffield.ac.uk; l.susmel@sheffield.ac.uk

Primary Supervisor: H. Askes – e-mail: h.askes@sheffield.ac.uk
Secondary Supervisor: L. Susmel – e-mail: l.susmel@sheffield.ac.uk

ABSTRACT. In this paper, the accuracy of gradient elasticity in estimating the fatigue strength of engineering components, characterised by the presence of stress risers and subjected to multiaxial high-cycle fatigue loadings, is assessed. In particular, a new approach, based on the combination of the Ru-Aifantis theory of gradient elasticity and the Theory of Critical Distances (TCD), is proposed for the fatigue assessment of notched metallic components. The proposed methodology represents an important step forward respect to the state of the art, allowing an accurate fatigue assessment of engineering components, by post-processing the relevant gradient-enriched stresses directly on the surface of the component, with evident advantages from a practical point of view.

KEYWORDS. Gradient elasticity; Theory of Critical Distances; Multiaxial Fatigue; Notch; Length Scale.

INTRODUCTION

Engineering components are often characterised by complex shapes, presenting different stress concentration features that strongly affect the fatigue behaviour of the materials being assessed. Therefore, an accurate stress analysis is essential to perform a reliable fatigue assessment of components containing stress risers.
Unfortunately, classical elasticity produces unphysically high stress values in the neighbourhood of stress concentration features, leading to non-accurate fatigue assessments. To overcome this problem and deliver accurate fatigue assessments, different theories have been proposed in the past. Amongst these, the Theory of Critical Distances, also known as TCD (for a complete overview see [1]), represents a very effective and accurate tool for the estimation of high-cycle fatigue strength of notched components. The TCD, originally proposed by Neuber [2] and Peterson [3] for the estimation of the high-cycle fatigue strength of notched components, is based on the assumption that a fatigue crack propagates when the range of the effective stress (function of a critical distance, considered a material constant) exceeds the plain fatigue limit of the material, for the relevant load ratio $R = \sigma_{min}/\sigma_{max}$.
Despite its undoubted accuracy and advantages, the use of the TCD for the fatigue assessment of mechanical components requires the knowledge of the failure location into the analysed body a priori, which is not a trivial task from a practical point of view.
However, a family of theories known as *gradient elasticity* has been shown to be able to remove the singularities from the stress fields or, more in general, to smooth the stresses, respectively, in the vicinity of sharp crack tips and stress

concentrators such as notches, etc. (see for example [4–6]). This ability has the great advantage of allowing a more accurate estimation of the stresses even at the tip of the stress concentrators, i.e. on the surface of the components, avoiding the need to predetermine the failure location into the material. Similarly to the TCD, gradient elasticity assumes that the relevant stress fields in the neighbourhood of crack/notch tips have to be calculated by directly including an internal length parameter (representative of the underlying microstructure) into the constitutive relations.
In this paper, a new methodology based on the combination of gradient elasticity, in particular the Ru-Aifantis theory (for a comprehensive overview see [5]), and the TCD is proposed. The accuracy and reliability of the proposed methodology in estimating the multiaxial high-cycle fatigue strength of notched components has been validated by using a large number of experimental results taken from the literature.

GRADIENT ELASTICITY

Gradient elasticity represents a family of theories which allows to take into account the influence of the underlying microstructure of the material on the global behaviour of a component. This is possible by enriching the constitutive relations by means of high-order gradients, of relevant state variables, accompanied by intrinsic length parameters.
In this paper, the theory developed by Aifantis and co-workers in the early 90s [7–9], and recently implemented in a unified finite element methodology [6], is considered. This theory consists in enriching the constitutive relations with the Laplacian of the strains as follows:

$$\sigma_{ij} = C_{ijkl}\varepsilon_{kl} - \ell^2\varepsilon_{kl,mm} \tag{1}$$

where σ_{ij} is the Cauchy's stress tensor, ε_{ij} is the infinitesimal strain tensor, C_{ijkl} is the elastic tensor and ℓ is the intrinsic length scale of the material. This leads to the following equilibrium equations:

$$C_{ijkl}u_{k,jl} - \ell^2 u_{k,jlmm} + b_i = 0 \tag{2}$$

where u_k are the displacements and b_i the body forces.
Eq. (2) represents a system of fourth-order partial differential equations (p.d.e.), whose implementation in a finite element framework is non-trivial due to the stringent continuity requirements [5]. However, Ru and Aifantis [9] proposed a theorem consisting in a factorisation of the derivatives, which allows the solution of Eq. (2) as two decoupled systems of second-order p.d.e., allowing a straightforward and effective C^0 finite element implementation [6].
The first step of the aforementioned theorem consists in the solution of the standard equations of classical elasticity

$$C_{ijkl}u^c_{k,jl} + b_i = 0 \tag{3}$$

where u^c_k are the classical (or local) displacements.

Using then as source term the local displacements u^c_k calculated from Eq. (3), it is possible to solve the following second system of p.d.e. in terms of stresses [4, 5, 10]

$$\sigma^g_{ij} - \ell^2\sigma^g_{ij,mm} = C_{ijkl}u^c_{k,l} \tag{4}$$

where σ^g_{ij} are the gradient-enriched (or non-local) stresses.

THEORY OF CRITICAL DISTANCES

As stated by Taylor [1], the TCD represents a family of methods, all characterised by two main common features: the use of linear elastic analysis and of a constant critical distance (characteristic of the material). All these methods assume that, under cyclic loading, the threshold condition for crack propagation is given by [11]:

$$\Delta\sigma_{eff} = \Delta\sigma_0 \tag{5}$$

where $\Delta\sigma_{eff}$ represents the range of the effective stress, which is function of the critical distance, L, while $\Delta\sigma_0$ is the plain fatigue limit range, related to the load ratio $R = \sigma_{min}/\sigma_{max}$.

The different approaches, followed to determine the range of the effective stress $\Delta\sigma_{eff}$, identify different versions of the TCD [11]. In particular, the Point Method (PM) represents the simplest approach and consists in applying the TCD as proposed by Peterson [3]. In this case the range of the effective stress $\Delta\sigma_{eff}$ is given by the following expression:

$$\Delta\sigma_{eff} = \Delta\sigma_y\left(\theta = 0, r = \frac{L}{2}\right) \tag{6}$$

where r and θ represent the local polar coordinates in a reference system centred at the notch tip. Furthermore, the critical distance L is defined as follows [12]:

$$L = \frac{1}{\pi}\left(\frac{\Delta K_{th}}{\Delta K_0}\right)^2 \tag{7}$$

where ΔK_{th} is the threshold value of the stress intensity factor range.

The TCD as just described can be applied only to notched components subjected to in-service Mode I fatigue loading. In order to extend its use to multiaxial situations, this approach has to be applied along with an appropriate multiaxial fatigue damage model [12, 13]. According to a systematic validation based on a large number of experimental results [12, 14, 15], the highest accuracy is obtained by applying the PM together with a bi-parametrical critical plane approach known as Modified Wöhler Curve Method (MWCM).

The Modified Wöhler Curve Method

The MWCM belongs to the family of the so-called *critical plane approaches*, where the critical plane is defined as the material plane experiencing the maximum shear stress amplitude, τ_a. The MWCM consists in estimating the multiaxial fatigue strength in terms of τ_a, by conveniently modifying the fatigue curves through a coefficient able to take into account the degree of multiaxiality of the load history as well as the damaging effect of non-zero mean stresses normal to the critical plane [12]. This coefficient, called *critical plane stress ratio*, ρ_{eff}, is defined as [16]:

$$\rho_{eff} = \frac{m \cdot \sigma_{n,m} + \sigma_{n,a}}{\tau_a} \quad \text{for} \quad \rho_{eff} < \rho_{lim} \quad \text{and} \quad \rho_{eff} = \rho_{lim} = \frac{\tau_{A,\infty}}{2\tau_{A,\infty} - \sigma_{A,\infty}} \quad \text{for} \quad \rho_{eff} \geq \rho_{lim} \tag{8}$$

where m is the mean stress sensitivity index, while $\sigma_{n,m}$ and $\sigma_{n,a}$ are, respectively, the mean value and the amplitude of the stress normal to the critical plane.

According to the MWCM, denoting with $\sigma_{A,\infty}$ and $\tau_{A,\infty}$, respectively, the fully-reversed uniaxial and torsional endurance limits extrapolated at N_A cycles to failure, the following equivalent shear stress can be defined:

$$\tau_{eq} = \tau_a - \left(\frac{\sigma_{A,\infty}}{2} - \tau_{A,\infty}\right) \cdot \rho_{eff} \tag{9}$$

Combining Gradient Elasticity with the TCD

One of the main unresolved problems of gradient elasticity theories is the identification of the length scale parameters. Although it is widely accepted that these parameters are somehow related to microstructural features of the material, a clear identification is still missing.

Inspired by the similarities shared by the Ru-Aifantis theory and the TCD, Susmel and co-workers [17] tried to formally

relate the Ru-Aifantis model and the TCD, finding a practical and effective relation between the internal length scale, ℓ, and the critical distance, L, in the case of cracked components:

$$\ell \approx \frac{L}{2\sqrt{2}} \tag{10}$$

Considering that both ℓ and L are intrinsic material properties (hence their values are independent of the geometry of the problem), in this paper, Eq. (10) has been used to relate the two length parameters also in the case of notched components.

VALIDATION THROUGH EXPERIMENTAL DATA – MULTIAXIAL FATIGUE LOADING

The accuracy and reliability of the proposed design approach were assessed by post-processing a large number of experimental data taken from the literature. The considered results were generated by testing, under in-phase and out-of-phase multiaxial fatigue loadings [12, 14, 18], metallic specimens containing different geometrical features. Table 1 summarises the experimental results used to perform the validation.
The analysed specimens can be subdivided into two families: shafts with shoulder fillet (SSF) for which, following Gough's experimental findings [19], the crack initiation was considered to occur at the junction of the fillet with the central part of the specimen, and circumferentially notched cylindrical bars (CNB) under in-phase and out-of-phase fully-reversed loadings. In order to assess its accuracy in taking into account the mean stress effect in fatigue, the proposed approach was also used to estimate the high-cycle fatigue strength of En3B [18] and S65A [19] notched samples subjected to biaxial fatigue loading with superimposed static stresses.
To be consistent with gradient elasticity, when the stress field is characterised by a certain gradient (in this case both bending and torsion), also the plain fatigue limits should be recalculated according to gradient elasticity. For this purpose the gradient-affected plain endurance limits $\sigma^{g}_{A,\infty}$ and $\tau^{g}_{A,\infty}$ were determined by analysing the plain bars presented in [19, 20] with the proposed methodology, using the ℓ-values reported in Table 1, under both pure bending and pure torsion.

Material	Ref.	R	$\sigma^{g}_{A,\infty}$ [MPa]	$\tau^{g}_{A,\infty}$ [MPa]	m	L [mm]	ℓ [mm]	Specimen Type[a]	Load Type[b]	r_n [mm]
SAE 1045	[20]	-1	303.1	175.5	-	0.159	0.056	SSF	B-T	5
Ck 45	[21]	-1	303.1	175.5	-	0.159	0.056	SSF	B-T	5
S65A	[19]	-1	581.6	369.7	0.37	0.056	0.020	SSF	B-T	0.838
0.4% C Steel	[19]	-1	325.1	203.1	-	0.178	0.063	CNB	B-T	0.005
3% Ni Steel	[19]	-1	337.2	201.9	-	0.144	0.051	CNB	B-T	0.005
3/3.5% Ni Steel	[19]	-1	330.6	252.6	-	0.516	0.182	CNB	B-T	0.01
Cr-Va Steel	[22]	-1	423.9	255.2	-	0.101	0.036	CNB	B-T	0.011
3.5% NiCr Steel (normal impact)	[22]	-1	530.5	346.4	-	0.150	0.053	CNB	B-T	0.022
3.5% NiCr Steel (low impact)	[22]	-1	502.5	320.2	-	0.109	0.039	CNB	B-T	0.022
NiCrMo Steel (75-80 tons)	[22]	-1	586.6	339.1	-	0.106	0.037	CNB	B-T	0.031
En3B	[18]	-1	346	266.5	0.22	0.048	0.017	CNB	Ax-T	0.2÷4.0

[a]SSF=cylindrical Shaft with Shoulder Fillet; CNB=Circumferential Notch in cylindrical Bar
[b]Ax=Axial loading; B=Bending; T=Torsion

Table 1: Summary of the experimental results generated under multiaxial fatigue loading.

To assess the accuracy of the proposed methodology in estimating the multiaxial high-cycle fatigue strength of notched components the following error was defined:

$$E_{\tau}[\%] = \frac{\tau^{g}_{eq} - \tau^{g}_{A,\infty}}{\tau^{g}_{A,\infty}} \cdot 100 \tag{11}$$

where τ^{g}_{eq} is obtained from Eq. (9) by using the gradient-enriched endurance limits, $\sigma^{g}_{A,\infty}$ and $\tau^{g}_{A,\infty}$, as well as the gradient-enriched critical plane stress ratio, ρ^{g}_{eff}, determined by substituting into Eq. (8) τ^{g}_{a}, $\sigma^{g}_{n,m}$ and $\sigma^{g}_{n,a}$, obtained by post-processing, through software Multi-FEAST (www.multi-feast.com), the gradient-enriched stress history determined at the crack initiation point.

In the performed analyses, the boundary conditions were taken as homogeneous essential for the first step (Eq. (3)), in order to restore the symmetry of the problem, and homogeneous natural throughout for the second step (Eq. (4)).

Figure 1 confirms that the proposed approach produces estimations mainly ranging in $\pm 20\%$ error interval (this holding true also for out-of-phase loading and under non-zero mean stresses). Furthermore, from Figure 1 it is possible to observe that the proposed multiaxial approach leads to highly accurate estimations also for simple nominal uniaxial cases.

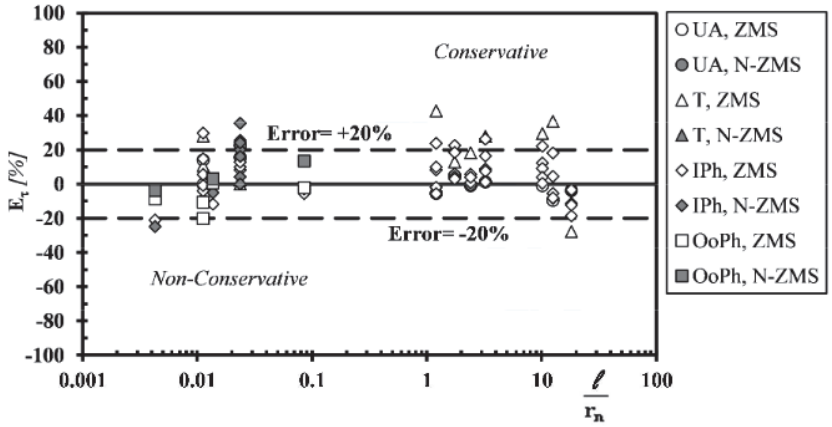

Figure 1: Accuracy of gradient elasticity applied along with the MWCM in estimating high-cycle fatigue strength of notched specimens subjected to uniaxial/multiaxial fatigue loading (UA=uniaxial loading; T=torsional loading; IPh=In-Phase loading; OoPh=Out-of-Phase loading; ZMS=Zero Mean Stress; N-ZMS=Non-Zero Mean Stress).

Conclusions

The present paper shows the effectiveness and accuracy of gradient elasticity and in particular of the Ru-Aifantis theory in estimating the fatigue strength of components presenting different types of stress concentration features and subjected to multiaxial high-cycle fatigue loadings. Thanks to the ability of gradient elasticity to smooth the stress field in the vicinity of stress risers, the proposed methodology allows the accurate estimation of the fatigue limit by considering the stress field directly at the assumed crack initiation point on the surface of the specimen. This leads to significant simplifications respect to many existing fatigue assessment approaches, which require the knowledge of the failure location into the assessed body a priori.

These results have important implications since, as soon as the length scale, ℓ, will be clearly identified, it will be possible to perform accurate fatigue assessments of notched components by simply using a gradient-enriched FE methodology, such as the one proposed in [6], without considering any linear elastic fracture mechanics (LEFM) concept. However, it has been shown that, in absence of a clear identification of the length scale, ℓ, the relation proposed in [17], based on well-known LEFM concepts, represents a good and practical approximation of the length scale.

Concluding, at the light of the results presented in the present paper, it is possible to state that the proposed approach can potentially become a powerful tool for the fatigue assessment and design of engineering components.

Acknowledgments

The author gratefully acknowledges 3DS Dassault Systemes (www.3ds.com) for fully supporting the present research investigation.

REFERENCES

[1] Taylor, D., The Theory of Critical Distances: A New Perspective in Fracture Mechanics. Elsevier, Oxford, UK, (2007).

[2] Neuber, H., Theory of notch stresses: principles for exact calculation of strength with reference to structural form and material. Springer Verlag, Berlin, (1958).

[3] Peterson, R. E., Notch-sensitivity, in G. Sines, J. L. Waisman (Eds.), Metal Fatigue, McGraw Hill, New York, (1958) 293–306.

[4] Askes, H., Morata, I., Aifantis, E. C., Finite element analysis with staggered gradient elasticity. Comput. Struct., 86(2008) 1266–1279. doi: 10.1016/j.compstruc.2007.11.002.

[5] Askes, H., Aifantis, E. C., Gradient elasticity in statics and dynamics: An overview of formulations, length scale identification procedures, finite element implementations and new results. Int. J. Solids Struct., 48(13)(2011) 1962–1990. doi: 10.1016/j.ijsolstr.2011.03.006.

[6] Bagni, C., Askes, H., Unified finite element methodology for gradient elasticity. Comput. Struct., 160(2015) 100–110. doi: 10.1016/j.compstruc.2015.08.008.

[7] Aifantis, E. C., On the role of gradients in the localization of deformation and fracture. Int. J. Eng. Sci., 30(10)(1992) 1279–1299. doi: 10.1016/0020-7225(92)90141-3.

[8] Altan, S. B., Aifantis, E. C., On the structure of the mode III crack-tip in gradient elasticity. Scripta Metallurgica et Materialia, 26(1992) 319–324.

[9] Ru, C. Q., Aifantis, E. C., A simple approach to solve boundary-value problems in gradient elasticity. Acta Mechanica, 101(1993) 59–68. doi: 10.1007/BF01175597.

[10] Askes, H., Gitman, I., Non-singular stresses in gradient elasticity at bi-material interface with transverse crack, Int. J. Fract., 156(2009) 217–222.

[11] Taylor, D., Geometrical effects in fatigue: a unifying theoretical model, Int. J. Fatigue, 21(1999) 413–420. doi: 10.1016/S0142-1123(99)00007-9.

[12] Susmel, L., Multiaxial Notch Fatigue: from nominal to local stress-strain quantities. Woodhead & CRC, Cambridge, UK (2009), ISBN: 1 84569 582 8.

[13] Susmel, L., Taylor, D., Can the conventional High-Cycle Multiaxial Fatigue Criteria be re-interpreted in terms of the Theory of Critical Distances?, Structural Durability & Health Monitoring, 2(2)(2006) 91-108.

[14] Susmel, L., A unifying approach to estimate the high-cycle fatigue strength of notched components subjected to both uniaxial and multiaxial cyclic loadings, Fatigue Fract. Engng. Mater. Struct., 27(5)(2004) 391–411.

[15] Susmel, L., Taylor, D., Two methods for predicting the multiaxial fatigue limits of sharp notches, Fatigue Fract. Engng. Mater. Struct., 26(2003) 821-833.

[16] Susmel, L., Multiaxial Fatigue Limits and Material Sensitivity to Non-Zero Mean Stresses Normal to the Critical Planes, Fatigue Fract. Engng. Mater. Struct., 31(2008) 295-309.

[17] Susmel, L., Askes, H., Bennett, T., Taylor, D., Theory of Critical Distances versus Gradient Mechanics in modelling the transition from the short to long crack regime at the fatigue limit. Fatigue Fract. Engng. Mater. Struct., 36(2013) 861–869. doi: 10.1111/ffe.12066.

[18] Susmel, L., Taylor, D., The Modified Wöhler Curve Method applied along with the Theory of Critical Distances to estimate finite life of notched components subjected to complex multiaxial loading paths, Fatigue Fract. Engng. Mater. Struct., 31(12)(2008) 1047-1064.

[19] Gough, H. J., Engineering Steels under Combined Cyclic and Static Stresses. In: Proc. Inst. Mech. Engrs., 160(1949) 417-440.

[20] Kurath, P., Downing, S. D., Galliart, D. R., Summary of non-hardened notched shaft round robin program, in G. E. Leese and D. F. Socie (Eds.), Multiaxial Fatigue. Society of Automotive Engineers, AE-14(1989) 13–32.

[21] Sonsino, C. M., Fatigue Behaviour of Welded Components Under Complex Elasto-Plastic Multiaxial Deformation, LBF-Bericht, Nr. 6078 (1994).

[22] Taylor, D., Wang, G., The validation of some methods of notch fatigue analysis. Fatigue Fract. Engng. Mater. Struct., 23(2000) 387–394.